

Numerical predictions and measurements of Reynolds normal stresses in turbulent pipe flow of polymers

P.R. Resende ^a, M.P. Escudier ^b, F. Presti ^b, F.T. Pinho ^{c,*}, D.O.A. Cruz ^d

^a Centro de Estudos de Fenómenos de Transporte, DEMEGI, Faculdade de Engenharia, Universidade do Porto, Rua Dr. Roberto Frias s/n, 4200-465 Porto, Portugal

^b Department of Engineering, University of Liverpool, Brownlow Street, Liverpool L69 3GH, UK

^c Centro de Estudos de Fenómenos de Transporte, DEM, Universidade do Minho Campus de Azurém, 4800-058 Guimarães, Portugal

^d Departamento de Engenharia Mecânica, Universidade Federal do Pará-UFPa Campus Universitário do Guamá, 66075-900 Belém, Pará, Brazil

Received 4 January 2005; received in revised form 5 August 2005; accepted 6 August 2005

Available online 27 September 2005

Abstract

An anisotropic low Reynolds number $k-\varepsilon$ turbulence model has been developed and its performance compared with experimental data for fully-developed turbulent pipe flow of four different polymer solutions. Although the predictions of friction factor, mean velocity and turbulent kinetic energy show only slight improvements over those of a previous isotropic model [Cruz, D.O.A., Pinho, F.T., Resende, P.R., 2004. Modeling the new stress for improved drag reduction predictions of viscoelastic pipe flow. *J. Non-Newt. Fluid Mech.* 121, 127–141], the new turbulence model is capable of predicting the enhanced anisotropy of the Reynolds normal stresses that accompanies polymer drag reduction in turbulent flow.

© 2005 Elsevier Inc. All rights reserved.

Keywords: Anisotropy of Reynolds normal stresses; Turbulence model; Experiments in polymer drag reduction; Pipe flow

1. Introduction

Although the topic of drag reduction in turbulent duct flow of dilute polymer solutions has been investigated extensively for some 50 years, thanks to recent developments in both computer technology and experimental techniques particularly significant progress has been made over the past 5 years. The increasing performance of computers now allows full direct numerical simulations (DNS) of turbulent flow of polymer solutions, at least at fairly low Reynolds numbers, using non-linear viscoelastic differential constitutive equations to represent the polymer contribution to the total stress, such as the Giesekus or FENE type models. Such calculations have been reported by Sureshku-

mar et al. (1997), Dimitropoulos et al. (1998) and more recently by Ptasiński et al. (2003), Housiadas and Beris (2004), Dubief et al. (2004) and Zhou and Akhavan (2003) while Graham (2004) provides a comprehensive review of more recent numerical investigations. For surfactant-based drag-reducing fluids DNS investigations have been carried out by Yu and Kawaguchi (2003) and by Yu et al. (2004) also using viscoelastic differential constitutive equations. Modern diagnostic techniques have been used to probe the relation between the flow dynamics and the polymer (additive) behavior and recently there have been new findings under the limiting conditions of maximum drag reduction. For example, the experiments of Ptasiński et al. (2001, 2003), of Warholic et al. (1999) and of Vlachogiannis and Hanratty (2004) reveal a massive deficit of Reynolds shear stress for such flows, although the recent DNS results of Dubief et al. (2004) and Li et al. (2004) emphasize the strong effect of data rate upon such a finding.

* Corresponding author.

E-mail addresses: resende@fe.up.pt (P.R. Resende), escudier@liv.ac.uk (M.P. Escudier), fpinho@dem.uminho.pt (F.T. Pinho), doac@ufpa.br (D.O.A. Cruz).

Nomenclature

a	parameter defined as $a \equiv 2 - n - p $	s_{ij}	fluctuating rate of deformation tensor
A_s	function in anisotropic model, Eq. (A.9)	S_{ij}	time-average rate of deformation tensor, defined in Eq. (12)
A^+	Van Driest's parameter, $A^+ = 26.5$, in Eq. (14)	S^*	second invariant of tensor S_{ij}^* , Eq. (A.7)
A_2	parameter of $\bar{\mu}_h$, $A_2 = 0.45$ in Eq. (10)	S_{ij}^*	normalized rate of deformation tensor, $S_{ij}^* \equiv S_{ij}k/\varepsilon$
A_ε	turbulence model parameter of $\bar{\mu}_h$, $A_\varepsilon = 10$	t	time
b_{ij}	anisotropy tensor, defined in Eq. (28)	u	local mean velocity
B	parameter of $\bar{\mu}_h$, $B \equiv \rho^m 2^{[(n-1)-m(n+1)]/2} \left[\frac{K_v K_\varepsilon}{A_\varepsilon^{p-1}} \right]^{1-m}$ in Eq. (10)	$\frac{u_i}{u^2}$	velocity vector component along coordinate x_i
B_1	parameter in Eq. (16)	U	axial Reynolds normal stress
C	turbulence model parameter in f_μ	U_b	axial mean velocity
C_0	parameter in anisotropic turbulence model	u_τ	bulk velocity
$\tilde{C}, C_\mu, C_{\varepsilon 1}, C_{\varepsilon 2}, C_{\varepsilon 4}$	isotropic turbulence model parameters	u_R	friction velocity
DR	drag reduction intensity	u_R	characteristic turbulent scaling velocity, defined in Eq. (16)
f	Darcy friction factor	u', v', w'	defined as $u' \equiv \sqrt{u'^2}$ and similarly for v' and w'
$f_{n,1}, f_{n,2}, f_{n,3}$	corrective non-Newtonian functions of anisotropic model, defined in Eqs. (21), (22), and (26)	$\frac{w^2}{w^2}$	tangential Reynolds normal stress
f_{S1}, f_{S2}	damping functions in anisotropic turbulence model, Eq. (A.5)	W_{ij}	time-average of the vorticity tensor, defined in Eq. (12)
f_t	damping function for turbulent diffusion of k and $\tilde{\varepsilon}$, defined in Eq. (19)	W^*	second invariant of tensor W_{ij}^* , Eq. (A.7)
f_v	damping function of molecular viscosity, $f_v = f_\mu$	W_{ij}^*	normalized vorticity tensor, $W_{ij}^* \equiv W_{ij}k/\varepsilon$
f_μ	damping function of eddy viscosity, defined in Eq. (14)	$-\rho \bar{u}\bar{v}$	Reynolds shear stress
$f_{\mu 2}, f_w$	damping function in anisotropic model, Eqs. (A.8) and (A.13)	$-\bar{u}_i \bar{u}_j$	Reynolds stress tensor, Eq. (11)
f_1, f_2	damping functions in $\tilde{\varepsilon}$ equation	x	axial coordinate
g	function in anisotropic model, Eq. (A.10)	y	distance measured from the wall
k	turbulent kinetic energy	y^+	wall coordinate, $y^+ \equiv u_\tau y/\nu_w$
K_ε	consistency index of Trouton ratio behavior in Eq. (8)	<i>Greek Symbols</i>	
K_v	shear viscosity consistency index in Eq. (8)	$\tilde{\alpha}_i$	parameter in anisotropic turbulence model
m	parameter of $\bar{\mu}_h$, $m \equiv (n + p - 2)/(n + p)$ in Eq. (10)	$\tilde{\beta}_2, \tilde{\beta}_3, \beta_{2,\text{wall}}, \beta_{3,\text{wall}}$	coefficients of non-linear stress-strain relation, defined in Eqs. (A.1) and (A.2)
m_c	Cross-model exponent, Eq. (1)	δ_{ij}	Kronecker symbol
n	shear viscosity power index, Eq. (8)	ε	rate of dissipation of turbulent kinetic energy
N_1	first normal-stress difference	$\tilde{\varepsilon}$	modified rate of dissipation of turbulent kinetic energy
\bar{p}	mean pressure	$\dot{\varepsilon}$	invariant measurement of the strain rate (time average value)
p	power index of Trouton ratio behavior, Eq. (8)	$\dot{\gamma}$	invariant measurement of the shear rate (time average value)
P_1, P_2	functions in anisotropic turbulence model, Eqs. (A.11) and (A.12)	η	parameter/function in anisotropic model, Eq. (A.6)
r	radial coordinate	η_v	shear (viscometric) viscosity, defined in Eq. (8)
R	pipe radius	λ	parameter in Cross-model, defined in Eq. (1)
Re_g	generalized Reynolds number, $Re_g \equiv \frac{\rho D^n U_b^{2-n}}{K_v 8^{n-1} [(3n+1)/4n]^n}$	ν_T	eddy viscosity
Re	wall Reynolds number, $Re \equiv \frac{\rho D U_b}{\bar{\mu}_w}$	ν_w	kinematic viscosity at the wall
R_T	turbulent Reynolds number, $R_T \equiv k^2/(\bar{v}\tilde{\varepsilon})$	ν	kinematic viscosity
S	invariant of the rate of deformation tensor	$\bar{\nu}$	time-average kinematic viscosity
S_B	parameter in anisotropic turbulence model, Eq. (A.4)	$\bar{\nu}^2$	radial Reynolds normal stress
S_W	modified strain variable, Eq. (A.3)	μ	molecular viscosity or viscosity in Cross-model (Eq. (1))
		$\bar{\mu}$	true time-average molecular viscosity, defined in Eq. (9)
		μ_0	zero shear rate viscosity in Cross model, Eq. (1)

μ_∞	infinite shear rate viscosity in Cross model, Eq. (1)	<i>Subscripts</i>	
$\bar{\mu}_h$	time-average molecular viscosity for high Reynolds number turbulence, defined in Eq. (10)	0	refers to zero shear rate
ρ	fluid density	∞	refers to infinite shear rate
σ_ε	turbulent Prandtl number for ε	w	based on wall conditions
σ_{ij}	stress tensor, Eq. (7)	<i>Superscript</i>	
σ_k	turbulent Prandtl number for k	+	designates quantities normalised with wall coordinates
τ	shear stress		
θ	tangential coordinate		
ζ	parameter/function in anisotropic model, Eq. (27)		

A number of theories to explain the drag-reduction phenomenon have been formulated over the years and mechanisms involving extensional viscosity attracted the attention of researchers from very early on. Although present-day researchers are more inclined to pursue an explanation on the basis of molecular relaxation time versus turbulent time scales, these are intimately related to extensional-flow behavior, especially the transient extensional viscosity and the mechanisms of vortex stretching. Unfortunately, there are as yet no techniques to measure reliably and accurately the extensional viscosity of the dilute and semi-dilute polymer solutions used in turbulent flow studies. In spite of this lack, Escudier et al. (1999) attempted to correlate the measured degree of drag reduction of various polymer solutions in fully-developed turbulent pipe flow in terms of an extensional-viscosity index estimated by opposed-jet rheometry. They reported a general tendency for an increase in drag reduction to correlate with increasing levels of estimated extensional viscosity. The recent development of the filament stretching rheometer (McKinley and Sridhar, 2002) and especially of capillary breakup systems (Stelzer et al., 2000; Entov and Hinch, 1997) promise to provide considerably more reliable techniques for estimating the extensional viscosity of dilute polymer solutions than the opposed-jet rheometer, but so far no research has been published correlating such data with turbulent-drag reduction.

On the numerical front, in spite of all the DNS research reported by the various groups using viscoelastic differential constitutive equations, no single-point turbulence closure has yet appeared in the literature. This deficiency is a consequence of the complexity of the problem, leading to a large number of time-averaged terms in the transport and constitutive equations that need to be modeled, and the difficulties of deducing adequate closures. These difficulties inspired Pinho (2003), Cruz and Pinho (2003) and Cruz et al. (2004) to develop a family of turbulence models from a different perspective: instead of adopting a differential viscoelastic constitutive equation from the outset, they took the generalized Newtonian constitutive equation and modified the viscosity function using the Trouton ratio to mimic the effects of strain-hardening on the turbulent flow characteristics of viscoelastic fluids. In this way they brought into the model an important extensional fluid

property of the fluid arguably related to drag reduction, while keeping to a minimum the changes in the time-averaged transport equations relative to those for a Newtonian fluid. This approach has the advantage of reducing the changes to classical Newtonian turbulent models, which today can be regarded as advanced tools benefiting from many years of development. In consequence, although the complete physics of a viscoelastic fluid is not well captured by the adopted constitutive equation, the number of assumptions and simplifications that need to be invoked to arrive at a closed set of equations is much reduced compared with what would appear in the more rigorous approach of using a truly viscoelastic differential model.

The philosophy just outlined has already enabled the development of a low Reynolds number k - ε turbulence model for viscoelastic fluids and in this paper a more sophisticated version is presented. A basic deficiency of the previous models of Cruz and Pinho (2003) and of Cruz et al. (2004) was the assumption that the turbulence was isotropic. As is well known, the turbulence structure in fully-developed pipe or channel flows is not isotropic even for a Newtonian fluid and the inclusion of polymer additives further enhances the anisotropy of the Reynolds stress tensor. This anisotropy can be tackled by a second-order scheme or, for simple flows, by the use of an anisotropic low Reynolds number version of a k - ε turbulence model.

The aim of the present work is to report on the modifications of an existing low Reynolds number, anisotropic k - ε turbulence model for Newtonian fluids which can be used to predict the increased levels of anisotropy found under drag-reducing conditions and to compare the predictions of this model with previously unreported measurements of the Reynolds normal stresses for fully-developed pipe flow of a range of viscoelastic, shear-thinning polymer solutions. Models for predicting Reynolds-stress anisotropy are non-linear and their proper development also requires validation against turbulent flows developing in the flow direction. Hitherto there have been no such data for viscoelastic fluids, which also includes characterization of their extensional and shear rheologies.

In Section 2 we report briefly on the experimental set-up and techniques used in the experimental flow programme

as well as on the fluid rheology. In Section 3 the governing equations for fully-developed turbulent pipe flow and the turbulence closure adopted for the Reynolds stress tensor are presented. The modifications to the existing anisotropic model (for which details are given in Appendix A) are presented in Section 4, with emphasis placed on some of the realizability problems. The original anisotropic model is presented in Appendix A. Predictions based upon the new turbulence model are compared in Section 5 with experimental data. The performance of this model is also assessed through predictions under limiting rheological conditions that were not investigated here experimentally.

2. Experimental set-up, techniques and fluid rheology

2.1. Experimental flowloop and instrumentation

The flow loop (at the University of Liverpool) used for the experiments is the same as that described by Escudier and Presti (1996). The test section consisted of 13 precision-bore borosilicate glass tubes (ID 100.4 ± 0.1 mm) each of length 1.027 m (± 3 mm) which gave an overall test-section length of 13.35 m and a length:diameter ratio of 133:1. Pressure drop along the test section was measured using a Validyne differential pressure transducer (DP15-26, 3448 Pa fsd) for which the accuracy was estimated to be better than ± 0.25 of fsd. A platinum resistance thermometer mounted just downstream of the test section was used to monitor the fluid temperature to an accuracy of ± 0.1 °C.

Measurements were made 107 pipe diameters from the pipe inlet of the radial distributions of the mean axial velocity and of the axial, radial and tangential turbulence intensities. These measurements were carried out in back scatter using a Dantec fibreflow laser Doppler anemometer (LDA) system for which the measurement volume has a principal axis in the radial direction of length 0.21 mm and diameter 0.02 mm. In view of the small size of the measurement volume, no correction was applied for the effect of velocity-gradient broadening. The probe head, housing both the transmitting and receiving optics, was mounted on a three axis traverse with a spatial resolution of 15 μ m. All measurements were biased according to residence time. The Fischer and Porter electromagnetic flowmeter incorporated in the flow loop was found to indicate flow rates to within 1% of values computed from the velocity profiles.

2.2. Fluid rheology

The fluids used in the present work were aqueous solutions of the following polymers:

- sodium carboxymethylcellulose (CMC), a high-viscosity grade supplied by Aldrich Chemical Company, concentration 0.25% by weight;

- xanthan gum (XG), a food grade supplied by the Kelco Division of Merck and Co, concentration 0.2% by weight;
- polyacrylamide (PAA), Separan AP273 supplied by Floerger, concentration 0.125% by weight.

In addition a blend of 0.09% CMC with 0.09% XG was used.

Each of these polymer solutions has been used extensively in previous investigations of drag reduction and other non-Newtonian fluid-flow behaviour (see e.g. Pinho and Whitelaw (1990) and Escudier et al. (1999), the new turbulence data reported here being derived from the same study as the drag-reduction data reported in the latter paper).

The shear viscosity and first normal-stress difference characteristics of the test fluids were determined using a Bohlin VOR controlled-stress rheometer with either a concentric cylinder (double gap), a cone-and-plate or a parallel-plate geometry. As can be seen from Fig. 1, the measured shear viscosity for each of the polymer solutions used is well represented by the Cross-model for a shear-thinning liquid:

$$\frac{\mu_0 - \mu}{\mu - \mu_\infty} = (\lambda \dot{\gamma})^{m_c} \quad (1)$$

The values for the four parameters in Eq. (1) for each of the working liquids are listed in Table 1. Although these rheological data are shown for a temperature of 20 °C, similar measurements were made over a range of temperatures so that the viscosity values used to evaluate Reynolds numbers correspond to the liquid temperature measured during the flow experiments. In a plot of the shear viscosity versus

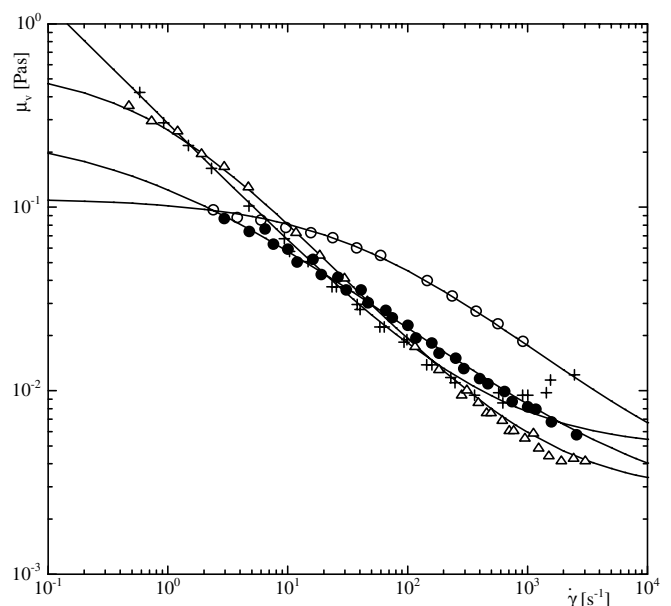


Fig. 1. Viscometric viscosity for (○) 0.25% CMC, (●) 0.09%/0.09% CMC/XG blend, (△) 0.2% XG, (+) 0.125% PAA. Solid lines curves represent the Cross-model.

Table 1
Cross-model parameters at 20 °C

Fluid	μ_0 (Pa s)	μ_∞ (Pa s)	λ (s)	m_c
0.25% CMC	0.112	0.00239	0.0214	0.595
0.09% CMC/0.09% XG	0.267	0.00200	1.34	0.512
0.2% XG	0.578	0.00276	1.30	0.724
0.125% PAA	29.6	0.00481	1090	0.664

shear rate in log–log coordinates, a Newtonian plateau at low shear rates is evident for the CMC solution. Otherwise, all fluids were found to exhibit almost power-law behaviour except at the highest shear rates ($>1000/s$) for PAA where the data were adversely affected by the onset of secondary flow.

At the concentrations used here, the first normal-stress differences for CMC, XG and CMC/XG were below the sensitivity of the rheometer even at the highest shear rates. However, as suggested by Barnes et al. (1989), at higher concentrations it was found that $N_1(\tau)$ followed a power-law master curve for each fluid, practically independent of concentration, from which it was possible to extrapolate to lower concentrations. This procedure is not ideal but has to suffice in the absence of either a direct measurement or a more sophisticated extrapolation algorithm. The data result in the empirical expressions

$$N_1 = 0.85\tau^{1.25} \quad 0.6\text{--}1.5\%\text{CMC} \quad (2)$$

$$N_1 = 0.97\tau^{1.47} \quad 1.0\text{--}1.5\%\text{XG} \quad (3)$$

$$N_1 = 1.35\tau^{1.18} \quad 0.4/0.4\text{--}1.5/1.5\%\text{CMC/XG} \quad (4)$$

According to Barnes et al., a recoverable shear (i.e., $N_1/2\tau$) greater than 0.5 indicates a highly elastic state. For the three polymer solutions considered here, this condition corresponds to shear stresses in excess of 1.9 Pa (CMC), 1.1 Pa (XG) and 0.2 Pa (CMC/XG).

For PAA the N_1 values were above the sensitivity limit of our rheometer and it was possible to obtain (N_1 versus $\dot{\gamma}$) data directly and these are well represented by

$$N_1 = 16.3\tau^{1.48} \quad 0.125\%\text{PAA} \quad (5)$$

so that 0.125% PAA can be said to be highly elastic for $\tau > 0.003$ Pa.

Unlike the normal-stress difference situation, it was possible to obtain a direct estimate of the extensional viscosity for each of the polymer solutions at the concentrations used in the flow experiments. These measurements were obtained using a Rheometrics RFX opposed-nozzle rheometer, the majority of measurements being made with nozzles of diameters 1, 3 and 5 mm. For each rheometer setting, at least three measurements were made and only those data retained which produced consistent values for extensional viscosity. At the highest strain rates ($>30 s^{-1}$) the elasticity ranking (in ascending order) was found to be CMC/XG, XG, CMC and PAA. At intermediate strain rates ($5 s^{-1} < \dot{\gamma} < 30 s^{-1}$), CMC fell below XG but remained above CMC/XG. For the lowest strain rates ($<5 s^{-1}$) it appeared that CMC would also fall below

CMC/XG. This elasticity sequence for strain rates between $5 s^{-1}$ and $30 s^{-1}$ was the same for all four liquids as that based upon the first normal-stress difference at low shear rates. At the highest shear and strain rates, the relative positions of CMC/XG and XG were reversed. The most anomalous observation was that XG appeared to be more elastic than PAA at very low shear rates. This trend is not totally unexpected since the solution of XG behaves as a gel at low rates of deformation and its structure breaks down in strong shear and/or extension (Walters, 1992). There are serious reservations about the opposed-jet technique and a more reliable technique is needed to determine reliable and accurate data for elongational viscosity.

3. Governing equations and turbulence model

The main equations to be solved for fully-developed turbulent pipe flow of a viscoelastic fluid are the Reynolds averaged continuity and momentum equations. The former is identical to that for a Newtonian fluid, while the latter is given by

$$-\frac{\partial \bar{p}}{\partial x_i} + \frac{\partial (2\bar{\mu}S_{ik} - \rho\overline{u_i u_k} + 2\overline{\mu' S_{ik}})}{\partial x_k} = 0 \quad (6)$$

Here and elsewhere, lower-case letters or a prime indicate fluctuations and upper-case letters or an overbar designate time-averaged quantities. In this work \bar{p} is the mean pressure and u_i is the velocity component in the x_i direction. Eq. (6) is based on the constitutive model adopted by Pinho (2003) to represent the fluid rheology,

$$\sigma_{ij} = 2\mu S_{ij} \quad (7)$$

where the viscosity μ is a function of invariants ($\dot{\gamma}, \dot{\epsilon}$) of the rate of deformation tensor, S_{ij} , as in Eq. (8)

$$\mu = \eta_v K_e [\dot{\epsilon}^2]^{\frac{n-1}{2}} = K_v (\dot{\gamma}^2)^{\frac{n-1}{2}} K_e [\dot{\epsilon}^2]^{\frac{n-1}{2}} \quad (8)$$

The first part in Eq. (8) (η_v) accounts for the dependence of the viscosity on shear rate, here using a power-law of consistency index K_v and power index n . The dependence on the strain rate is accounted for by the second part which is dimensionless and represents the Trouton ratio, as explained in detail elsewhere (Pinho, 2003; Cruz and Pinho, 2003). The invariants of the rate of deformation tensor are $\dot{\gamma} = \sqrt{3}\dot{\epsilon}$ and $\dot{\epsilon}$, both defined in Pinho (2003). Basically, $\dot{\gamma}$ quantifies the shear rate of deformation whereas $\dot{\epsilon}$ represents the normal rate of deformation, often called strain rate. Parameters K_e and p are dimensionless fitting parameters to the variation of Trouton ratio with $\dot{\epsilon}$.

The numerical values of the four rheological parameters used here are the same as in Cruz et al. (2004) and listed in Table 2.

The average molecular viscosity $\bar{\mu}$ in Eq. (6) is the combination in Eq. (9) of the purely shear viscosity contribution for the near wall region (η_v) and the high Reynolds number time-average molecular viscosity contribution

Table 2

Parameters of viscosity law used to fit the shear and extensional viscosity data in Escudier et al. (1999) (from Cruz et al., 2004)

Fluid	K_v (Pa s ^{<i>n</i>})	n	K_e	p
0.25% CMC	0.2639	0.6174	2.0760	1.2678
0.09% CMC/0.09% XG	0.15178	0.5783	2.1833	1.1638
0.2% XG	0.2701	0.4409	3.8519	1.2592
0.125% PAA	0.2491	0.425	8.25	1.4796

($\bar{\mu}_h$) far from the wall deduced by Pinho (2003) and given in Eq. (10)

$$\bar{\mu} = f_v \bar{\mu}_h + (1 - f_v) \eta_v \tag{9}$$

$$\bar{\mu}_h = (C_\mu \rho)^{\frac{3m(m-1)A_2}{8+3m(m-1)A_2}} 2^{\frac{4m(m-1)A_2}{8+3m(m-1)A_2}} k^{\frac{6m(m-1)A_2}{8+3m(m-1)A_2}} \varepsilon^{\frac{[8-3(m-1)A_2]m}{8+3m(m-1)A_2}} B^{\frac{8}{8+3m(m-1)A_2}} \tag{10}$$

f_v is the molecular viscosity damping function and k and ε represent the turbulent kinetic energy and its rate of dissipation, respectively.

There are three stresses in Eq. (6): the molecular stress $2\bar{\mu}S_{ik}$; the Reynolds shear stress $-\rho\bar{u}_i\bar{u}_k$, here modeled by the anisotropic expression of Eq. (11) and which constitutes the main contribution of this work so far as the turbulence model is concerned; and the additional non-Newtonian stress $2\bar{\mu}'s_{ik}$ recently modeled by Cruz et al. (2004).

$$\begin{aligned} -\bar{u}_i\bar{u}_j &= 2v_T S_{ij} - \frac{2}{3}k\delta_{ij} \\ &- k\left(\tilde{\beta}_2 f_{n,1} + C_w \tilde{\beta}_{2,\text{wall}} f_{n,3}\right)\left(S_{ik}^* S_{kj}^* - \frac{1}{6}S^{*2}\delta_{ij}\right) \\ &- k\left(\tilde{\beta}_3 f_{n,2} + C_w \tilde{\beta}_{3,\text{wall}} f_{n,3}\right)\left(W_{ik}^* S_{kj}^* - S_{ik}^* W_{kj}^*\right) \end{aligned} \tag{11}$$

The non-linearity in Eq. (11) comes from the dependence on the mean flow kinematic tensors S_{ij} and W_{ij} , which represent the rate of deformation and vorticity tensors as defined in Eq. (12).

$$S_{ij} = \frac{1}{2}\left(\frac{\partial U_i}{\partial x_j} + \frac{\partial U_j}{\partial x_i}\right), \quad W_{ij} = \frac{1}{2}\left(\frac{\partial U_i}{\partial x_j} - \frac{\partial U_j}{\partial x_i}\right) \tag{12}$$

The asterisks in Eq. (11), and elsewhere, indicate normalised values ($S_{ij}^* = S_{ij}k/\tilde{\varepsilon}$ and $W_{ij}^* = W_{ij}k/\tilde{\varepsilon}$) and $S^* = \sqrt{2S_{ij}^*S_{ij}^*}$. The 1/6 factor in Eq. (11) should be used instead of 1/3 as in Eq. (19) of Park et al. (2003), see also Apsley and Leschziner (1998).

The model adopted to calculate the Reynolds stress tensor is that of Park et al. (2003) for Newtonian fluids, without the third-order terms, but modified by functions $f_{n,1}$ to $f_{n,3}$ which are discussed in the next section. In this equation, the second-order terms provide the anisotropy of the normal-stress components in fully-developed pipe flow. Since we have adopted an isotropic eddy viscosity there is no contribution from the quadratic terms to the shear stress in fully-developed pipe flow, which therefore remains unmodified. The third-order terms are important in the

context of flows with streamline curvature, swirl, separation and flow redevelopment. They are not considered here for two reasons: first, our objective is the prediction of the Reynolds normal stresses in fully-developed pipe flow of viscoelastic fluids with the emphasis on predicting their enhanced anisotropy under drag-reducing conditions; secondly, for a proper validation of a full anisotropic model (i.e., including the third-order terms), we would need the results of fluid dynamics experiments for these fluids (or other viscoelastic fluids for which there are shear and extensional viscosity measurements) in several such flows. Unfortunately no such data are available in the literature. Apsley and Leschziner (1998) provide a description of various non-linear k - ε models for Newtonian fluids and the corresponding responses in various flows. The other details of the linear and quadratic terms of the original model of Park et al. (2003) are presented in Appendix A, whereas the discussion of its modifications for viscoelastic fluids is postponed to Section 4. In the remainder of this section we complete the turbulence model by presenting the so-called isotropic contribution, without further details since these were discussed previously (cf. Cruz and Pinho, 2003; Cruz et al., 2004).

For the eddy viscosity in Eq. (11) we adopt the previous isotropic model (Cruz and Pinho, 2003) given by the Prandtl–Kolmogorov equation

$$v_T = C_\mu f_\mu \frac{k^2}{\tilde{\varepsilon}} \tag{13}$$

with k and $\tilde{\varepsilon}$ to be determined via appropriate transport equations. The modified rate of dissipation of turbulent kinetic energy $\tilde{\varepsilon}$ is used in low Reynolds number models to change the wall boundary condition for numerical purposes, and is related to the true dissipation rate by $\varepsilon = \tilde{\varepsilon} + D$. As discussed in Cruz and Pinho (2003), lack of universal behavior in the wall region for viscoelastic fluids requires calculations to be made right up to the wall, i.e., a low Reynolds number model. For the damping function f_μ we adopt the expression deduced by Cruz and Pinho (2003), given in Eq. (14), and optimized by Cruz et al. (2004) with $C = 70$. Note also that we assume $f_v = f_\mu$.

$$\begin{aligned} f_\mu &= \left\{ 1 - \left[1 + \left| \frac{1-n}{1+n} \right| y^+ \right]^{-|1+n/1-n/A^+|} \right\} \\ &\times \left\{ 1 - \left[1 + \left| \frac{p-1}{3-p} \right| y^+ C^{\frac{1-p}{2-p}} \right]^{-|3-p/p-1/A^+|} \right\} \end{aligned} \tag{14}$$

where y^+ is the wall coordinate normalised by the wall viscosity ($y^+ \equiv u_\tau y/v_w$).

Finally, for fully-developed pipe flow, the additional non-Newtonian stress in the momentum equation $2\bar{\mu}'s_{sr}$ is modeled according to Cruz et al. (2004), by

$$2\bar{\mu}'s_{sr} = \tilde{C} \frac{K_v K_e}{A_e^{p-1}} \left[\frac{\rho C_\mu f_\mu \frac{k^2}{\tilde{\varepsilon}} \left(\frac{dU}{dr}\right)^2}{2\bar{\mu}} \right]^{\frac{p+n-2}{2}} \sqrt{C_\mu f_\mu \frac{k^2}{\tilde{\varepsilon}} \frac{1}{L_c} \frac{dU}{dr} \sqrt{\left|\frac{dU}{dr}\right|}} \tag{15}$$

where the parameter \tilde{C} is defined as $\tilde{C} \equiv (1 - C_S)^{p+n-2} - 1$, $C_S = +3.0$, $L_c = u_R^3/\varepsilon$ and the velocity scale u_R matches inner and outer velocity scales according to Eq. (16) using $B_1 = 4$.

$$u_R^2 = \frac{k}{\left[\left[e^{-(k/u_\tau^2)^{B_1}} - 1 \right] \right]^{1/B_1}} \quad (16)$$

The transport equations for the turbulent kinetic energy (Eq. (17)) and its rate of dissipation (Eq. (18)) are modified versions of those used by Cruz et al. (2004), here presented in their simplified form for fully-developed pipe flow

$$0 = \frac{1}{r} \frac{\partial}{\partial r} \left[r \left(\bar{\mu} + f_t \frac{v_T}{\sigma_k} \right) \frac{\partial k}{\partial r} \right] - \rho \overline{u_i u_j} S_{ij} - \rho \varepsilon - 2 \overline{\mu' s_{sr}} \frac{\partial U}{\partial r} \quad (17)$$

$$0 = \frac{1}{r} \frac{\partial}{\partial r} \left[r \left(\bar{\mu} + f_t \rho \frac{v_T}{\sigma_\varepsilon} \right) \frac{\partial \tilde{\varepsilon}}{\partial r} \right] - \rho f_1 C_{\varepsilon 1} \frac{\tilde{\varepsilon}}{k} \overline{u_i u_j} S_{ij} - \rho f_2 C_{\varepsilon 2} \frac{\tilde{\varepsilon}^2}{k} + \bar{\mu} v_T (1 - f_\mu) \left(\frac{\partial^2 U}{\partial r^2} \right)^2 + C_{\varepsilon 4} \frac{v_T}{\sigma_\varepsilon \bar{v}} \frac{\partial \tilde{\varepsilon}}{\partial r} \frac{\partial \bar{\mu}}{\partial r} \quad (18)$$

These two equations have been modified relative to the previous model of Cruz et al. (2004) by the inclusion of function f_t in the turbulent diffusion term, which is modeled by invoking the gradient diffusion hypothesis, and a change in the numerical values of parameters σ_k and C_μ . Previously σ_k was taken as unity, but for Newtonian fluids it was found that this leads to too low a contribution of turbulent diffusion to the balance of k close to walls and too high a contribution away from walls (Nagano and Shimada, 1993). However, merely reducing σ_k leads to large differences between predictions and DNS results away from a wall. The solution to this problem is the introduction of an apparent variable diffusion parameter $\sigma_k^* (= \sigma_k/f_t)$ via function f_t . This function also improves the predictions for viscoelastic fluids and so the original form of the function of Park and Sung (1995)

$$f_t = 1 + 3.5 \exp \left[-(R_T/150)^2 \right] \quad (19)$$

was used. We also changed the value of σ_k from 1.0 to 1.1 to improve the predictions, as suggested by Nagano and Shimada (1993) and Park and Sung (1995) (σ_k is usually between 1.0 and 1.4). C_μ was also modified from 0.09 to 0.084 (and so remains within the accepted range of values) to improve the predictions of mean flow quantities for Newtonian fluids, although for viscoelastic fluids its impact is small given the more important role of f_μ (Cruz and Pinho, 2003).

The other damping functions present in the $\tilde{\varepsilon}$ -equation, f_1 and f_2 , are the same as used previously in conventional low Reynolds number turbulence models, namely $f_1 = 1$ and $f_2 = 1 - 0.3 \exp(-R_T^2)$. In a similar way, a variable turbulent diffusion coefficient $\sigma_\varepsilon^* (= \sigma_\varepsilon/f_t)$ was introduced into the $\tilde{\varepsilon}$ -equation. The turbulent Reynolds number R_T in Eq. (19) is given by $R_T \equiv \frac{k^2}{\bar{v} \varepsilon}$. The numerical values for the remaining parameters are listed in Table 3.

Table 3
Values of some parameters of the k - ε model

C_μ	$C_{\varepsilon 1}$	$C_{\varepsilon 2}$	$C_{\varepsilon 4}$	σ_k	σ_ε	A^+
0.084	1.45	1.90	1.0	1.1	1.3	26.5

4. Anisotropic turbulence closure

Once the transport equations for k and $\tilde{\varepsilon}$ have been solved, the Reynolds normal stresses can be calculated individually through Eq. (11). The non-linear part of this equation was modified with the non-Newtonian functions $f_{n,1}$, $f_{n,2}$ and $f_{n,3}$ to account for the fluid rheology, and in particular to increase the anisotropy of the Reynolds normal stresses with drag reduction, in agreement with experimental observations. The three functions improve the predictive capability of the model, while ensuring realizability constraints.

It is important to realize that the complexity of this model stems from the fact that it was deduced originally for separated flows of a Newtonian fluid and so is a rather general model. Here, of course, we are using it for the simpler situation of fully-developed pipe flow, the only case well documented in the literature both in terms of fluid dynamics as well as shear and extensional rheology (cf. Escudier et al., 1999; Cruz and Pinho, 2003). Future developments of this model, for which inclusion of cubic terms in the strain rate is needed to calculate the Reynolds stresses, will require data for flows with separation, streamline curvature and swirl of fluids which are well characterized in terms of both shear and extensional viscosities.

This non-linear model is able to predict anisotropy of the Reynolds normal stresses and an increase of the turbulence anisotropy with increasing drag reduction due to fluid rheology (with a reduction in n and an increase in p), when the corrective functions $f_{n,1}$, $f_{n,2}$ and $f_{n,3}$ are unitary. This is so because the non-linear model is already influenced by the non-Newtonian rheology via its dependence on the modified distributions of k and $\tilde{\varepsilon}$, which are appropriately affected by the fluid rheology through the isotropic part of the model. However, the use of the corrective functions can significantly improve the quality of predictions in terms of the Reynolds normal stresses and their anisotropy.

The viscoelastic functions have different roles: $f_{n,3}$ ensures realizability of the model when going from Newtonian to non-Newtonian fluids whereas the other functions are designed to improve the performance of the model. Specifically, $f_{n,2}$ corrects the distribution of \bar{v}^2 and has two contributions: $f_{n,21}$ decreases \bar{v}^2 near the wall, while $f_{n,22}$ increases \bar{v}^2 away from the wall. Finally, $f_{n,1}$ is used to correct $\overline{w^2}$ all the way across the pipe. Note that $\overline{u^2}$ does not require any correction since it already increases with drag reduction (when normalised with wall quantities). However, the unmodified non-linear model reduces \bar{v}^2 and $\overline{w^2}$ excessively, leading to unphysical negative values under certain conditions, or insufficiently thus demanding corrections that are performed by the viscoelastic correc-

tive functions. The main realizability problem lies with the radial normal stress which is the lowest of the three Reynolds normal stresses. For pure shear flow, realizability imposes the following inequality on this stress component:

$$\left[\frac{(\tilde{\beta}_3 f_{n,2} + C_W \tilde{\beta}_{3,\text{wall}} f_{n,3})}{2} - \frac{(\tilde{\beta}_2 f_{n,1} + C_W \tilde{\beta}_{2,\text{wall}} f_{n,3})}{12} \right] \leq \frac{2}{3} \left(\frac{\partial U}{\partial r} \frac{k}{\bar{\epsilon}} \right)^{-2} \quad (20a)$$

whereas for the tangential component we have the less restrictive condition.

$$\frac{(\tilde{\beta}_2 f_{n,1} + C_W \tilde{\beta}_{2,\text{wall}} f_{n,3})}{4} \left(\frac{\partial U}{\partial r} \frac{k}{\bar{\epsilon}} \right)^2 \leq 1 \quad (20b)$$

The main problem lies near the wall and basically this is controlled by function $f_{n,3}$, which complements the roles of $\tilde{\beta}_2$, $\tilde{\beta}_3$, $\tilde{\beta}_{2,\text{wall}}$ and $\tilde{\beta}_{3,\text{wall}}$ already introduced by Park et al. (2003) to ensure realizability with Newtonian fluids. The three non-Newtonian corrective functions were deduced empirically with the help of limiting theoretical fluids (fluids with a constant shear viscosity ($n = 1$) and different degrees of strain-hardening of the Trouton ratio ($p > 1$) and shear-thinning viscous fluids ($n < 1$) with a constant Trouton ratio of 3 ($p = 1$)) after invoking three assumptions: (i) for Newtonian fluids ($p = n = 1$) the non-linear model must reduce to that of Park et al. (2003), i.e., $f_{n,1} = f_{n,2} = f_{n,3} = 1$; (ii) the Reynolds-stress anisotropy must increase with drag reduction (i.e., as n decreases below 1 and/or p increases above 1), with the effects of p much stronger than those of n , in agreement with the corresponding effects upon drag reduction quantifiers (friction factor and mean velocity) (see Cruz and Pinho, 2003); (iii) realizability must be ensured for all values of n and p leading to values of the friction factor of the order of those predicted by Virk's maximum drag reduction asymptote and positive normal Reynolds stresses with $u^2 > w^2 > v^2$.

To arrive at the expressions for the corrective functions below, we also tried to improve as much as possible the predictions of the Reynolds normal stresses for the various fluids for which experimental data are reported in this work. If a is defined by $a \equiv |2 - n - p|$, the corrective functions take the form:

$$f_{n,1} = \left(0.9a \frac{1 + 0.9a}{K_e} \right)^{-1.7a} \quad (21)$$

$$f_{n,2} = [f_{n,21} + f_{n,22}]^{\frac{1.75(p-n)+2K_e a}{3.6+a}} \quad (22)$$

$$f_{n,21} = (0.8 + 0.0048R_T)^{0.7} \left[\frac{f_{n,211}}{y^+} \right]^{0.454(p-n+K_e a)^{-0.4665}} \quad (23)$$

$$f_{n,211} = 8 \times 10^6 \left[0.94 \frac{p}{n} + a \left(\frac{3.6n}{K_e p} + 0.85K_e \right) + \frac{0.15 \frac{p}{n}}{0.85(p-n) + 0.01} + \frac{0.15(p-n)}{0.85K_e a + 0.01} \right]^{-12.603} \quad (24)$$

$$f_{n,22} = \frac{K_e a (5y^+)^{0.01}}{1.95 - p + n} \quad (25)$$

$$f_{n,3} = \left(0.5a + \frac{1 - 0.1a}{0.8(K_e + a) + 0.2} \right)^{a^{0.05}} \quad (26)$$

To discuss the realizability issue we start by analysing Eq. (20a). For a Newtonian fluid, the functions presented by Park et al. (2003) ensure that the model always yields physically realistic values, as in the example shown by the two upper curves of Fig. 2. The solid line represents the right-hand side (RHS) of Eq. (20a) for a water flow at $Re = 42,900$ and we can see that the use of Park et al.'s β functions ensures the left-hand side (LHS) is always below that upper limit. However, for elastic fluids this may not be the case, as can be seen in the three bottom curves: the solid line again represents the RHS but for the flow of 0.125% PAA at $Re = 42,900$, the long dashed line represents the LHS of Eq. (20a) when the corrective functions are switched off (i.e., $f_{n,1} = f_{n,2} = f_{n,3} = 1$) and the short dashed line represents the LHS with the corrective functions included. When the corrective functions are switched off realizability is not being enforced near the edge of the viscous sublayer and the LHS slightly exceeds the upper limit. Also, for other fluids and/or Reynolds numbers for which drag reduction is higher, the difference between the dashed and solid lines is larger and leads to negative radial Reynolds normal stresses. This abnormal situation is corrected with the corrective viscoelastic functions adopted here (short dashes).

The main problem is in the viscous sublayer, the region affected by $f_{n,3}$ and, since the transport equations of momentum, turbulent kinetic energy and its dissipation

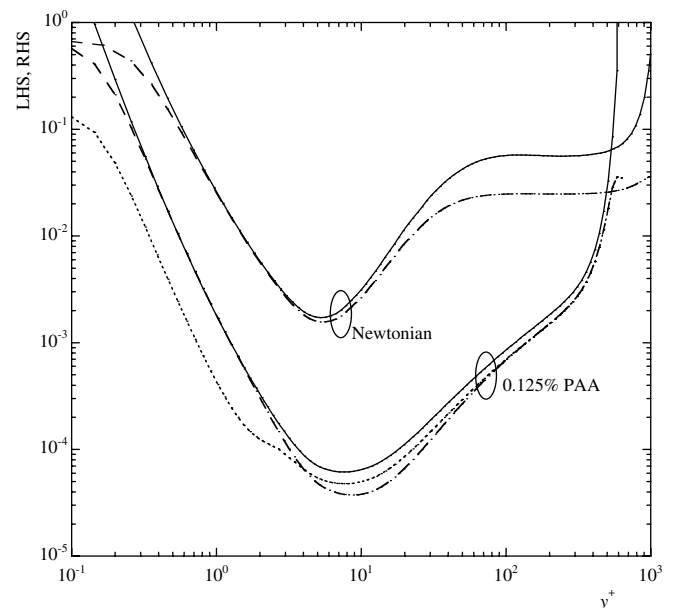


Fig. 2. Comparison between right-hand side (—) and left-hand side (---) of realizability Eq. (20a) for the turbulent pipe flow of water and 0.125% PAA solution at $Re = 42,900$: (—) ($f_{n,3} = 1$), (---) ($f_{n,3}$ from Eq. (26)).

rate are independent of the non-linear part of the Reynolds stress model (for fully-developed pipe or channel flows), the LHS of Eq. (20a) is represented by a single curve for each fluid in Fig. 2. Once $f_{n,3}$ is known it is possible to determine maximum values for the corrective functions $f_{n,1}$ and $f_{n,2}$ required not to violate realizability. Function $f_{n,1}$ has a more direct impact upon $\overline{w^2}$ but it also affects $\overline{v^2}$ and so its form changes the limits of $f_{n,2}$ and vice versa. These cross-effects have been analysed extensively and Eqs. (21)–(26) ensure both realizability and also improved predictions for all the fluids considered in this work as well as for fluids having different parameters n , p and K_e covering a wider range of values than those considered here.

To illustrate the impact of rheology on realizability limits, we show the effects of the rheological parameters K_e , p and n upon the limiting values of function $f_{n,2}$ in Fig. 3 when functions $f_{n,1}$ and $f_{n,3}$ are given by Eqs. (21) and (26), respectively. The limit depends on the Reynolds number and for specific values of Re or of Re_g the data show that conditions leading to increased drag reduction (strain-hardening of the Trouton ratio and/or shear-thinning of the viscometric viscosity) reduce the range of realizability. In the case of parameter p , the effect is basically the limiting value of $f_{n,2}$ in the buffer and inner log-law re-

gions whereas a decrease in n also reduces drastically the limiting value of $f_{n,2}$ at high values of y^+ . However, this is not as dramatic as might be thought because it is unlikely that such high values of y^+ would ever be reached with polymer solutions.

Function $f_{n,1}$, on the other hand, affects the negative term in Eq. (20a) which widens conditions of realizability, but if it is too large it will reduce excessively the tangential normal stress possibly leading to negative values (cf. Eq. (20b)).

5. Results and discussion

This section is divided into two parts. First, we assess the capability of the present anisotropic turbulence model to predict fully-developed turbulent pipe flow of a Newtonian fluid by comparing its predictions with data from the literature. In the second part we investigate the capability of the model to predict the Reynolds normal stresses for the flow of non-Newtonian fluids and here we consider two cases: (i) flows of theoretical fluids for which there are no data on the individual Reynolds stresses, but which are useful to investigate trends and, (ii) flows for which we have experimental data for the four polymer solutions discussed in Section 2.

The numerical simulations were carried out with a modified finite-volume code originally developed by Younis (1987) for boundary-layer flows of a Newtonian fluid. For fully-developed flow the mesh requires only one cell in the longitudinal direction, provided the axial pressure gradient is corrected according to Patankar and Spalding (1972), and 199 cells from wall-to-wall distributed non-uniformly across the pipe, ensuring at least 12 control volumes within the viscous sublayer ($y^+ < 5$), thus providing mesh independent results for all fluids.

5.1. Newtonian fluids

In Figs. 4–6 we present the results of simulations for the flow of a Newtonian fluid and compare with correlations from the literature and with data from Durst et al. (1995). These latter data correspond to pipe flow at a Reynolds number of 7430 which was low enough to allow accurate measurements of the Reynolds normal stresses very close to the wall.

The variation of the Darcy friction factor with Reynolds number is plotted in Fig. 4. The predictions compare well with the Blasius equation and the differences relative to the model of Cruz et al. (2004) stem from the different value now used for the eddy viscosity coefficient ($C_\mu = 0.084$ compared with 0.09) and the different treatment of turbulent diffusion of k and ε . The experimental measurements of Durst et al. (1995) exceed the Blasius equation by 6% which those authors considered to represent good agreement. The corresponding axial mean velocity profiles in wall coordinates at $Re = 7430$ are plotted in Fig. 5. Except near the pipe centerline, the predictions of

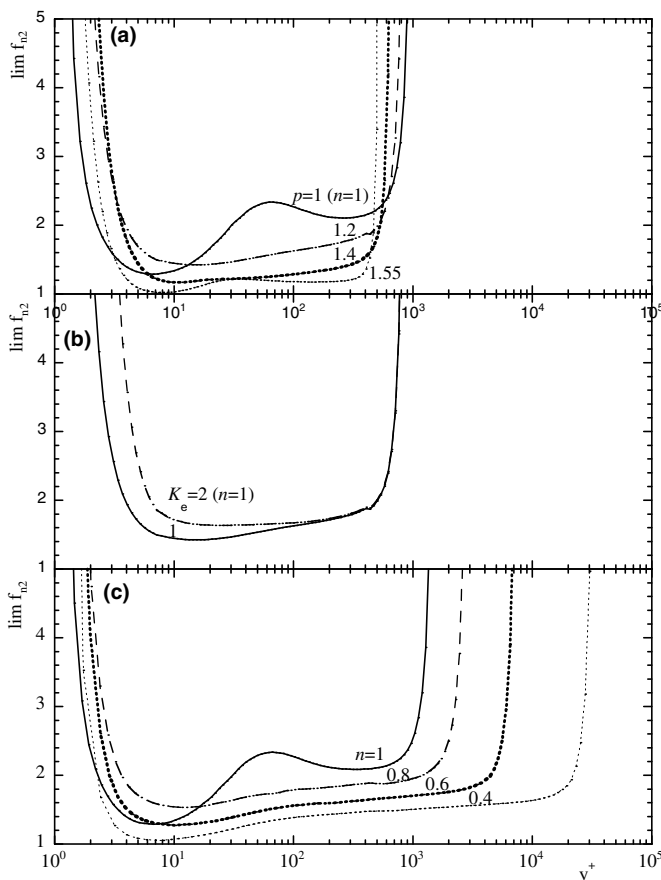


Fig. 3. Effect of the fluid properties p , K_e and n on the maximum limit value of $f_{n,2}$ to ensure realizability: (a) effect of p ($n=1$, $K_e=1$, $Re=42,770$); (b) effect of K_e ($p=1.2$, $n=1$, $Re=42,770$); (c) effect of n ($p=1$, $K_e=1$, $Re_g=68,140$).

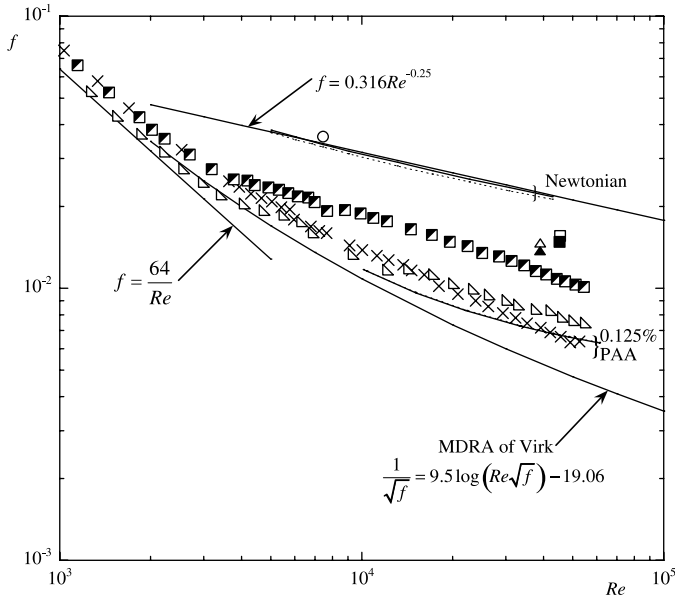


Fig. 4. Predictions and measurements of the Darcy friction coefficient for fully-developed pipe flow. Newtonian fluid: (○) data of Durst et al. (1995), (---) Cruz et al. (2004), (—) this model; 0.125% PAA: (×) data of Escudier et al. (1999), (---) Cruz et al. (2004), (—) this model; 0.2% XG: (△) data of Escudier et al. (1999), (△) Cruz et al. (2004), (▲) this model; 0.09%/0.09% CMC/XG: (■) data of Escudier et al. (1999), (□) Cruz et al. (2004), (■) this model.

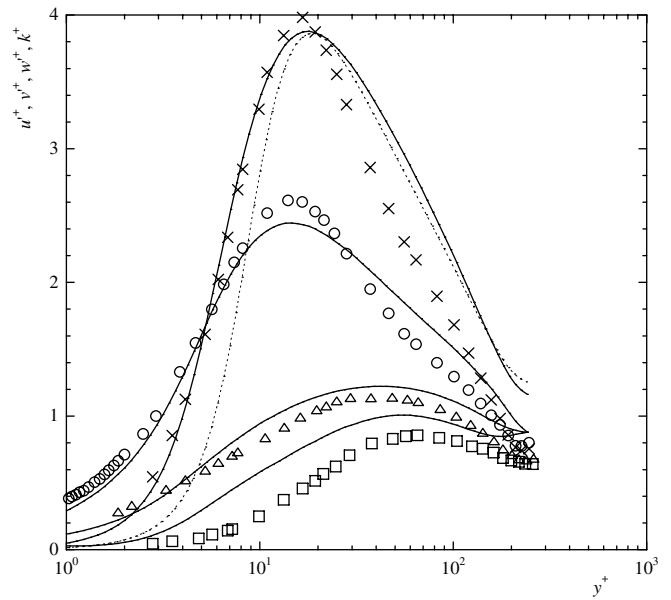


Fig. 6. Profiles of the normalised Reynolds normal stresses and turbulent kinetic energy in wall coordinates for fully-developed turbulent pipe flow of Newtonian fluid ($Re = 7430$): (○) u^+ , (□) v^+ , (△) w^+ ; (×) k^+ data of Durst et al. (1995); (—) this model; (---) predictions of k^+ by model of Cruz et al. (2004).

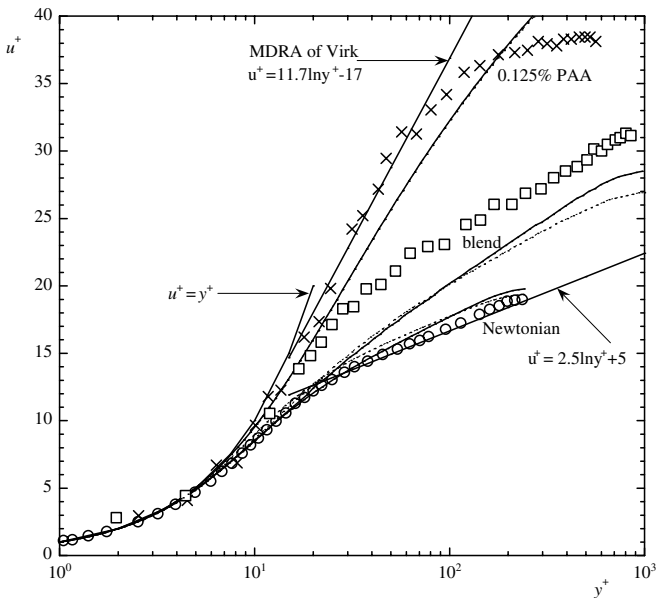


Fig. 5. Profiles of axial mean velocity in wall coordinates for fully-developed turbulent pipe flow: Newtonian fluid ($Re = 7430$): (○) data of Durst et al. (1995), (---) Cruz et al. (2004), (—) this model; 0.125% PAA ($Re = 42,900$): (×) data of Escudier et al. (1999), (---) Cruz et al. (2004), (—) this model; blend ($Re = 45,300$): (□) data of Escudier et al. (1999), (---) Cruz et al. (2004), (—) this model.

the present turbulence model are closer to the log-law and to the data of Durst et al. (1995) than those of Cruz et al. (2004). Note that the experimental data of Durst et al. agree with the DNS predictions of pipe flow of Kim

et al. (1987) at the same Reynolds number. The slight over-predictions of the log-law by both turbulence models is due to the low Reynolds number of the flow in combination with the still overprediction of turbulent diffusion in the outer region of the flow. Note that function f_t used (Eq. (19)) was calibrated by Park and Sung (1995) for channel flow, thus explaining some of the discrepancies observed in pipe flow.

It is in the prediction of turbulent-flow quantities that the new model is clearly superior to the model of Cruz et al. (2004). As can be seen from Fig. 6, for the turbulent kinetic energy, the changes in the isotropic part of the model (parameter C_μ and especially turbulent diffusion) have improved the predictions in the near-wall region between the wall and the turbulence peak at $y^+ \approx 18$ where there is now a good collapse between predictions and the measurements of Durst et al. (1995). In contrast to the isotropic model of Cruz et al. (2004), the present model is able to predict the anisotropy of the Reynolds normal stresses and this figure also compares these predictions with the measurements of Durst et al. (1995). For the axial component, this model predicts the near wall behavior well whereas for the tangential component there is a slight over-prediction. For the radial stress the over-prediction is greater, but in all cases the locations of the peak stresses are correct. Away from the wall, the differences are greater because the prediction of k is less successful.

Although the anisotropic model of Park et al. (2003) does a good job at predicting the channel flow DNS data of Moser et al. (1999), when solved together with its own isotropic contribution, here the predictions of the Reynolds

stress distributions in pipe flow are not as good, but it is important to realize that the isotropic part of the present model for Newtonian fluids is a modified version of that suggested by Nagano and Hishida (1987), ie it is not a fully optimized model on the basis of DNS data.

5.2. Non-Newtonian fluids

Calculations for two classes of fluid are analysed: first a series of theoretical fluids corresponding to limiting values of the rheological parameters n , p and K_e , and aimed at investigating their effect on the predictive capability of the turbulence model, and secondly previously unreported experimental data from the thesis of Presti (2000) for aqueous solutions of 0.125% PAA, 0.25% XG, 0.25% CMC and a blend of 0.09%/0.09% of XG/CMC.

5.2.1. Theoretical cases

The first theoretical case is that of the purely viscous, shear-thinning power-law fluid where the Trouton ratio is kept constant ($p = 1$). The Darcy friction factor is plotted in Fig. 7 (circles) as a function of the generalized Reynolds number (Re_g) introduced by Dodge and Metzner (1959) and, as with the previous model of Cruz and Pinho (2003) where more extensive comparisons are made, the level of drag reduction is overpredicted relative to Dodge and Metzner’s empirical Eq. (27) (solid lines).

$$\frac{1}{\sqrt{f}} = \frac{2}{n^{0.75}} \log \left[Re_g \left(\frac{f}{4} \right)^{1-n/2} \right] - \frac{0.2}{n^{1.2}} \quad (27)$$

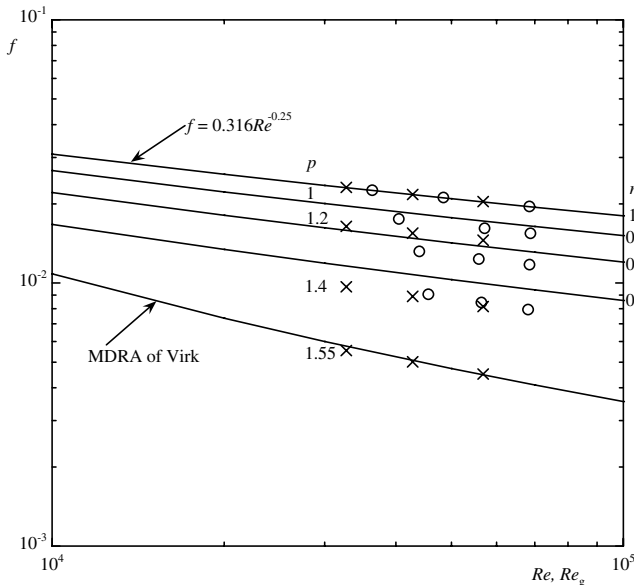


Fig. 7. Darcy friction factor: (○) variation of f with generalized Reynolds number (Re_g) and n for power-law fluids and comparison with the correlation of Dodge and Metzner (1959) (corrected on page 212 of Skelland, 1967); (×) variation of f with wall Reynolds number (Re) and p for Trouton ratio thickening fluids ($n = 1$, $K_e = 1$) in fully-developed turbulent pipe flow.

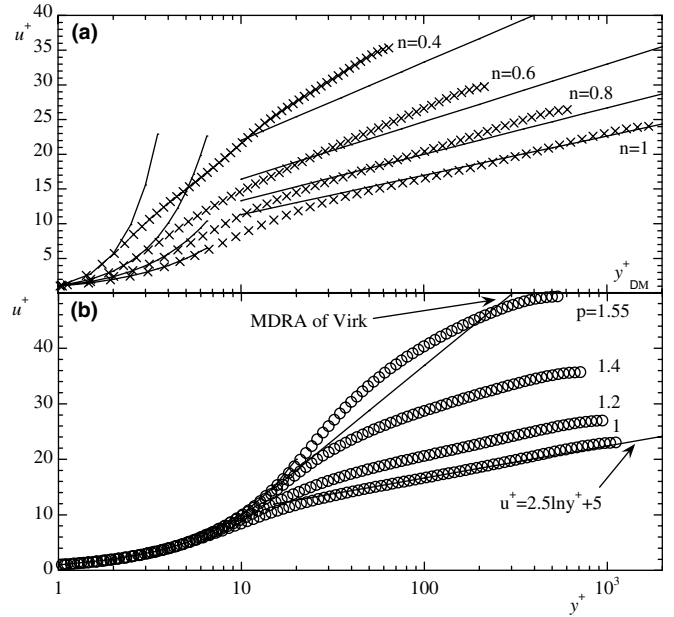


Fig. 8. Mean axial velocity distribution in wall coordinates in fully-developed turbulent pipe flow: (a) (×) power-law fluids ($Re_g = 68,500$) as a function of n , (—) correlation of Dodge and Metzner (1959) (corrected on page 212 of Skelland, 1967); (b) (○) Trouton ratio thickening fluids ($Re = 42,770$) as a function of p ($n = 1$, $K_e = 1$).

Both in terms of friction factor and mean velocity (the latter plotted in Fig. 8a) the predictions are similar to those of Cruz and Pinho (2003). The solid lines in Fig. 8a represent the velocity profile of Dodge and Metzner (1959) corrected by Skelland (1967).

In Fig. 9 the three normal components of the anisotropy tensor (Eq. (28)) are plotted against the wall coordinate.

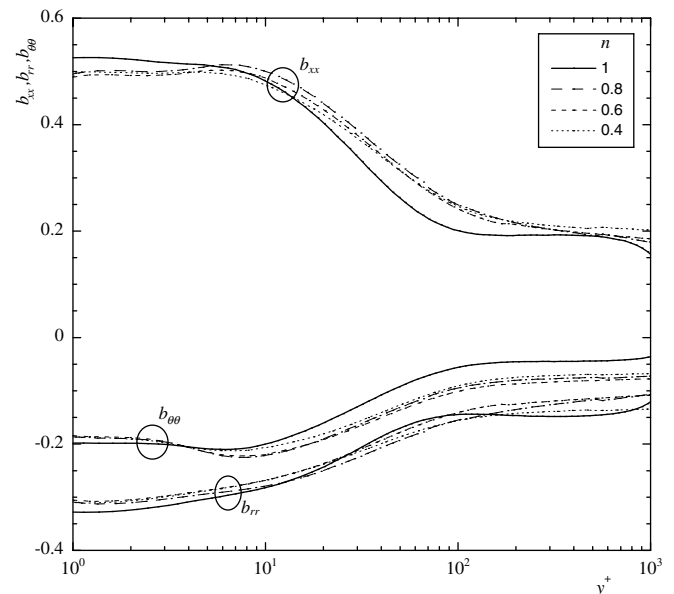


Fig. 9. Predictions of the distribution of the Reynolds normal-stress anisotropy for power-law fluids ($Re_g = 68,500$).

$$b_{ij} = \frac{\overline{u_i u_j}}{2k} - \frac{1}{3} \delta_{ij} \quad (28)$$

Three different types of behavior can be identified: within the viscous sublayer, shear-thinning slightly favours isotropy, reducing the highest normal component (b_{xx}) and increasing the two smaller components (b_{rr} and $b_{\theta\theta}$). In the center of the pipe (not shown) all profiles tend to zero (isotropy) since this turbulence model leads to Reynolds-stress isotropy when the rate of deformation is zero. In the most important intermediate (log-law) region, which include the peak turbulence and main turbulence production zones, there is clearly an increase in Reynolds-stress anisotropy with shear-thinning, especially for b_{xx} and $b_{\theta\theta}$. For the radial component, b_{rr} , the behavior is mixed. In terms of the corresponding rms velocities normalised in wall coordinates (not shown here because of space limitations) all components increase with shear-thinning, especially the axial component, which explains the higher values of b_{xx} . In any case, the amount of drag reduction due to pure shear-thinning is always rather small, but taking all components of b_{ij} into account it can be concluded that there is an increase in Reynolds-stress anisotropy with shear-thinning.

The second limiting case, of more interest here, is that of constant shear viscosity fluids with strain-hardening of the Trouton ratio, quantified by the exponent p . This is the fluid property underlying the main drag reduction effect and, in Fig. 7, the variation of the friction factor with p (crosses) is plotted as a function of the wall Reynolds number (Re). The figure includes now the maximum drag reduction asymptote (MDRA) of Virk which is attained by this model for p -values of around 1.55. The corresponding axial velocity profiles in wall coordinates are shown in Fig. 8b and Virk’s MDRA for velocity is also attained for $p = 1.55$. We note that Virk’s MDRA is not a true asymptote, but is in fact an envelope of experimental data. As p is progressively increased, the log-law is shifted upwards and at higher levels of drag reduction there is also an increase in the slope of the log-law region, until a maximum slope is reached for $p = 1.55$.

As expected, the effect of p on Reynolds-stress anisotropy is considerably stronger than that of n , since drag reduction is also more strongly affected by p than by n . The three normal components of the anisotropy tensor are plotted in Figs. 10 and, in the intermediate region between $y^+ \approx 10$ and the vicinity of the pipe center, there is an intense increase in b_{xx} and a decrease in both b_{rr} and $b_{\theta\theta}$. As already mentioned, at the centerline the model is unable to predict anisotropy because all components of the rate of deformation tensor go to zero. In the viscous sublayer p reduces anisotropy but the effect is quite small. This near wall behavior results from the different ways the various Reynolds stresses increase with wall distance. Inspection of the variations of the individual Reynolds normal stresses when normalised in wall coordinates (not shown here for conciseness) show a large increase in the axial component and small increases in the tangential and

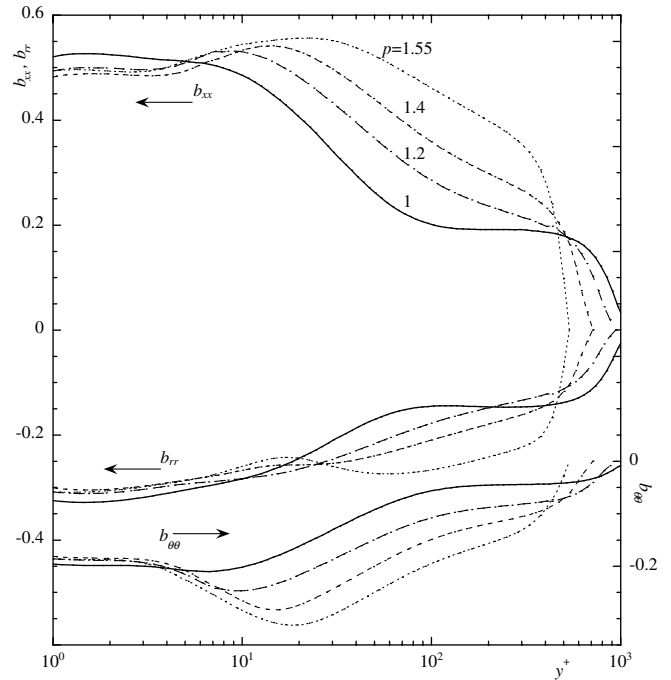


Fig. 10. Predictions of the Reynolds stress anisotropy for Trouton ratio thickening fluids ($Re = 42,770$).

radial components (the increase of the former is more than twice that of the tangential component and more than three times that of the radial component). However, when normalising with the bulk velocity, the radial and tangential rms velocities indeed decrease. The location of each Reynolds-stress peak value moves away from the wall as p progressively increases and the peaks also broaden.

5.2.2. Comparisons with experimental data

We start by presenting results for the 0.125% PAA solution, the fluid used to calibrate the isotropic part of the turbulence model by Cruz and Pinho (2003) and Cruz et al. (2004). It is important to remember that the calibration of the turbulence model was carried out only on the basis of the friction-factor data for this fluid. Since modifications to the isotropic part of the model were introduced in this work, for completeness we present here the comparison between the predicted and measured friction factors. This is followed by comparisons between the predicted and measured mean velocity, turbulent kinetic energy and finally the individual Reynolds normal stresses.

In Figs. 4 and 5 we compare the experimental fRe and u^+ versus y^+ data of Escudier et al. (1999) for 0.125% PAA with the predictions from the isotropic $k-\epsilon$ model of Cruz et al. (2004) and those from the new anisotropic model described here in Section 4. As with the theoretical fluids of the previous section, for this fluid the differences between the predictions of these two quantities by the two turbulence models are negligible. For the turbulent kinetic energy (not shown), both turbulence models again lead to similar predictions.

Regarding the Reynolds normal stresses, in Fig. 11 we compare the experimental data for 0.125% PAA with the predictions of the non-linear model without and with the corrective functions. Even in the absence of the viscoelastic corrections, the model captures the qualitative variations in all stresses and the differences between the behaviors of the Newtonian (cf. Fig. 6) and the 0.125% PAA solution, except very close to the wall where the radial stress exceeds the tangential stress. However, the differences between experimental data and predictions in Fig. 11 are not too different from the corresponding differences in Fig. 6 for Newtonian fluids. By switching on the corrective functions the predictions improve significantly, especially those of the radial and tangential components. This is not totally surprising because the predictions of the turbulent kinetic energy were already found to be good with the isotropic model (cf. Cruz et al., 2004) and the main contributor to k is $\overline{u^2}$, i.e., the predictions of this component could not be too much in error.

The predictions of friction factor and mean velocity for the 0.25% CMC solution are basically identical to those shown in Cruz et al. (2004) and were in good agreement with the experimental data. Similarly to Cruz et al. for the turbulent kinetic energy the predicted profile is shifted away from the wall, although otherwise the values are correct. As already remarked, the main contribution to k comes from the axial Reynolds normal stress, so for this component the pattern just described for k is observed in Fig. 12. In contrast to the PAA solution the predictions of $\overline{v^2}$ are always lower than those of $\overline{w^2}$ even close to the

wall and regardless of whether the corrective functions are switched on or off. Nevertheless, when these functions are used the predictions are improved, as expected.

Both the PAA and the CMC solutions are flexible molecules, whereas the remaining two fluids contain semi-rigid molecules of xanthan gum. Although the new model improves the predictions of drag reduction for the 0.2% XG and CMC/XG blend solutions relative to the model of Cruz et al. (2004), see Fig. 4, there still remains a significant difference relative to the experimental friction-factor data. Nevertheless, an improvement in the prediction of the friction coefficient implies an improvement in the prediction of the mean velocity profile for both fluids (shown for the blend in Fig. 5). In terms of the predictions of the Reynolds stresses for 0.2% XG, Fig. 13 shows that the turbulence model again predicts the stress anisotropy reasonably well with the functions switched off and improves them with the functions switched on. The underestimation of u'^+ ($u'^+ \equiv \sqrt{\overline{u^2}/u_\tau}$) reflects the underestimation of k that can be seen in Cruz et al. (2004). Although the prediction of $f-Re$ was improved relative to the previous turbulence model, the predicted peak value of k^+ is now slightly lower than that by Cruz et al.

Finally, for the 0.09%/0.09% CMC/XG blend Fig. 14 shows similar features to those reported above: fair predictions of all Reynolds normal stresses when the corrective functions are off, good predictions of v'^+ and w'^+ when using the corrective functions, but under-prediction of the peak u'^+ reflecting the deficiency in predicting the correct drag reduction and the corresponding peak value of k^+ .

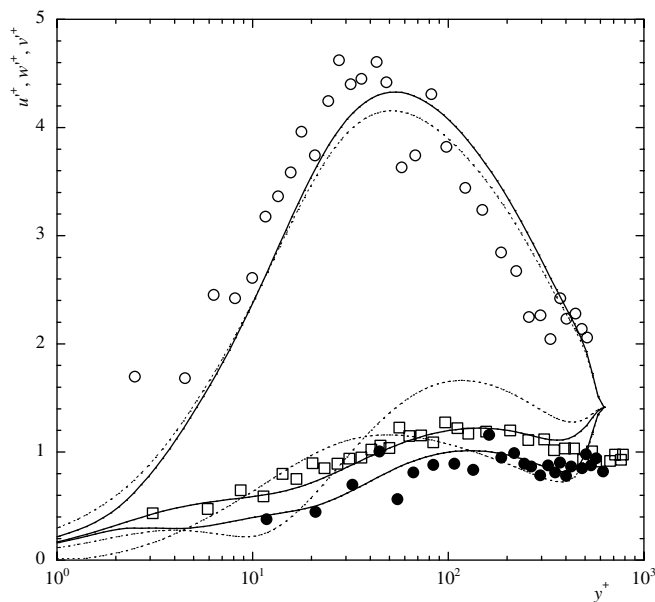


Fig. 11. Reynolds normal stresses for turbulent pipe flow ($Re = 42,900$) of 0.125% PAA (\circ) u'^+ , (\square) w'^+ , (\bullet) v'^+ : experimental data; (---) this model when corrective functions are switched off ($f_{n1} = f_{n2} = f_{n3} = 1$); (—) this model when corrective functions are switched on (f_{n1}, f_{n2}, f_{n3} given by Eqs. (21)–(26)).

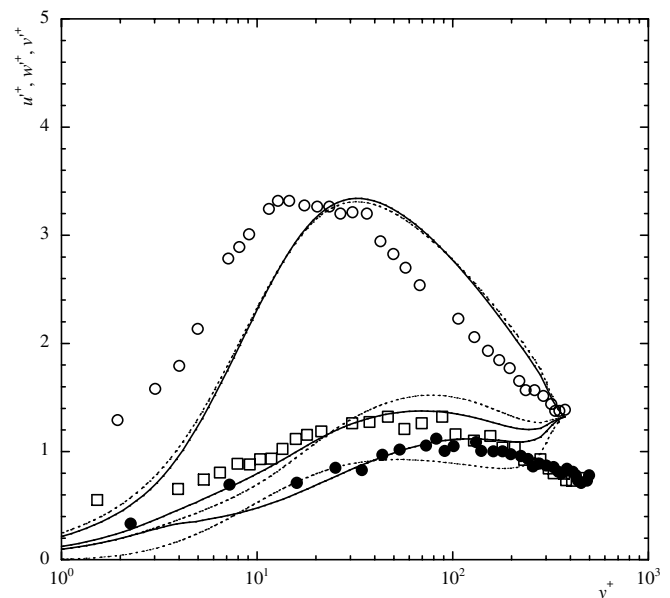


Fig. 12. Reynolds normal stresses for turbulent pipe flow ($Re = 16,600$) of 0.25% CMC. (\circ) u'^+ , (\square) w'^+ , (\bullet) v'^+ : experimental data; (---) this model with corrective functions switched off; (—) this model when corrective functions are switched on.

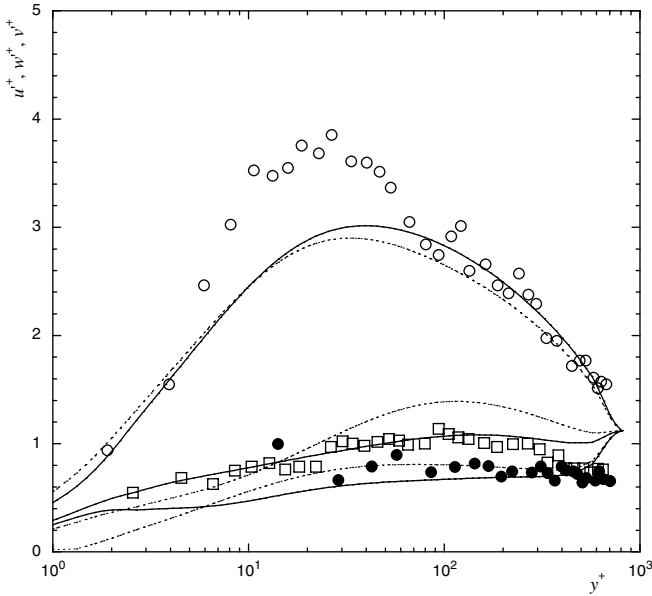


Fig. 13. Reynolds normal stresses for turbulent pipe flow ($Re = 39,000$) of 0.2% XG. (○) u'^+ , (□) w'^+ , (●) v'^+ : experimental data; (---) this model with corrective functions switched off; (—) this model when corrective functions are switched on.

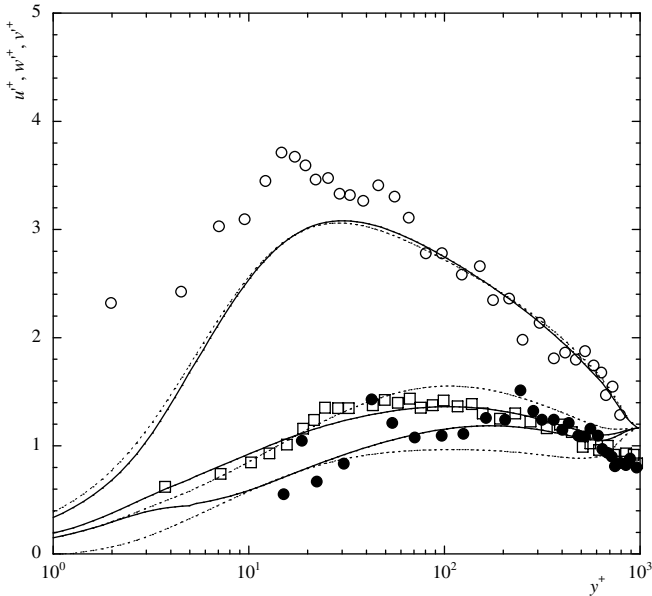


Fig. 14. Reynolds normal stresses for turbulent pipe flow ($Re = 45,200$) of 0.09%/0.09% CMC/XG blend. (○) u'^+ , (□) w'^+ , (●) v'^+ : experimental data; (---) this model with corrective functions switched off; (—) this model when corrective functions are switched on.

6. Conclusions

The low Reynolds number $k-\varepsilon$ turbulence model of Cruz et al. (2004) for viscoelastic polymer solutions has been extended to predict anisotropy of Reynolds normal stresses by modifications based on the model of Park et al. (2003) for turbulent flow of Newtonian fluids. The isotropic part of the model has also been modified and shown to improve

the predictions of the friction factor, the mean velocity and the turbulent kinetic energy. To assess the performance of the model, new measurements of the three Reynolds normal stresses are presented for four different polymer solutions which complement the data reported in Escudier et al. (1999).

The measurements confirm the usual increase in axial Reynolds normal stresses with drag reduction, and the corresponding dampening of the radial and tangential components of the Reynolds stress tensor. These effects were more intense with the solution of PAA, which has the most flexible and longest molecule of those investigated.

The anisotropic part of the turbulence model proposed here was found to be capable of predicting the increased anisotropy of the Reynolds normal stresses, but some realizability problems had to be overcome by the inclusion of corrective functions, which also improved the performance of the model.

Acknowledgements

The authors gratefully acknowledge funding of FEDER via research contracts POCTI 37699/EQU/2001 and POC-TI 37711/EME/2001 awarded by FCT, Portugal. Helpful discussions with Prof. B.A. Younis, University of California at Davis, are also acknowledged.

Appendix A

The anisotropic turbulence model of Park et al. (2003) was calibrated with the help of available DNS data for fully-developed channel flow of a Newtonian fluid. This model is given by Eq. (11) and the various functions appearing in its non-linear terms take the following forms:

$$\tilde{\beta}_2 = C_\mu f_{S1} f_w^2 \quad \tilde{\beta}_3 = C_\mu f_{S2} f_w^2 \quad (A.1)$$

$$\tilde{\beta}_{2,\text{wall}} = (1 - f_w) 2.5 \frac{S_B}{S_W} \quad \tilde{\beta}_{3,\text{wall}} = (1 - f_w) \left(1.8 \frac{S_B}{S_W} - \tilde{\beta}_3 \right) \quad (A.2)$$

$$S_W = 1 + [\max(S^*, W^*)]^2 \quad (A.3)$$

$$S_B = 2S_{\text{lm}}^* S_{\text{lm}}^* (1 - \delta_{\text{lm}}) / S^{*2} \quad (A.4)$$

$$f_{S1} = \frac{1 + \eta_s f_{\mu 2}}{1 + 4\eta_s + 4\eta_s^2} \quad f_{S2} = \frac{1 + \eta_s f_{\mu 2}}{1 + \eta_s + 8\eta_s^2} \quad (A.5)$$

$$\eta_s = C_\mu \max(\eta, \zeta) \quad \eta = f_w S^* \quad \zeta = f_w W^* \quad (A.6)$$

$$S^* = \sqrt{2S_{ij}^* S_{ij}^*} \quad W^* = \sqrt{2W_{ij}^* W_{ij}^*} \quad (A.7)$$

Function $f_{\mu 2}$ is given by Eq. (A.8) and requires the quantities defined in Eqs. (A.9)–(A.12).

$$f_{\mu 2} = \frac{5(1 + g)}{(g^2 + C_\mu g^3 + A_S)} \quad (A.8)$$

with

$$A_S = \tilde{\alpha}_3^2 \zeta^2 - \frac{\tilde{\alpha}_2^2 \eta^2}{3} \quad (A.9)$$

Table A.1
Parameters used in the anisotropic model

C_0	$\tilde{\alpha}_1$	$\tilde{\alpha}_2$	$\tilde{\alpha}_3$
2.4	-0.48	-0.375	-0.8

$$g = \begin{cases} \frac{C_0}{3} + (P_1 + \sqrt{P_2})^{1/3} + \text{sign}(P_1 - \sqrt{P_2})|P_1 - \sqrt{P_2}|^{1/3}, & P_2 \geq 0 \\ \frac{C_0}{3} + 2(P_1^2 - P_2)^{1/6} \cos\left(\frac{1}{3} \arccos\left(\frac{P_1}{\sqrt{P_1^2 - P_2}}\right)\right), & P_2 < 0 \end{cases} \quad (\text{A.10})$$

$$P_1 = C_0 \left[\frac{C_0^2}{27} - \frac{(A_S + \tilde{\alpha}_1 \eta^2)}{6} + \frac{1}{2} \right] \quad (\text{A.11})$$

$$P_2 = P_1^2 - \left[\frac{C_0^2}{9} - \frac{(A_S + \tilde{\alpha}_1 \eta^2)}{3} \right] \quad (\text{A.12})$$

Although the determination of f_w in a general flow requires the solution of a Helmholtz-type elliptic equation, as explained in Park et al. (2003), for fully developed duct flow the equation reduces to the Van Driest function used by Patel et al. (1985) with the Van Driest parameter taking on the value of 42, thus leading to

$$f_w = 1 - \exp\left(-\frac{y^+}{42}\right) \quad (\text{A.13})$$

The numerical values of the other parameters in the model are listed in Table A.1.

References

- Apsley, D.D., Leschziner, M.A., 1998. A new low-Reynolds-number nonlinear two-equation turbulence model for complex flows. *Int. J. Heat Fluid Flow* 19, 209–222.
- Barnes, H.A., Hutton, J.F., Walters, K., 1989. *An Introduction to Rheology*. Elsevier, Amsterdam.
- Cruz, D.O.A., Pinho, F.T., 2003. Turbulent pipe flow predictions with a low Reynolds number $k-\epsilon$ model for drag reducing fluids. *J. Non-Newt. Fluid Mech.* 114, 109–148.
- Cruz, D.O.A., Pinho, F.T., Resende, P.R., 2004. Modeling the new stress for improved drag reduction predictions of viscoelastic pipe flow. *J. Non-Newt. Fluid Mech.* 121, 127–141.
- Dimitropoulos, C.D., Sureshkumar, R., Beris, A.N., 1998. Direct numerical simulation of viscoelastic turbulent channel flow exhibiting drag reduction: effect of the variation of rheological parameters. *J. Non-Newt. Fluid Mech.* 79, 433–468.
- Dodge, D.W., Metzner, A.B., 1959. Turbulent flow of non-Newtonian systems. *AIChE J.* 5 (2), 189–204.
- Dubief, Y., White, C.M., Terrapon, V.E., Shaqfeh, E.S.G., Moin, P., Lele, S.K., 2004. On the coherent drag-reducing and turbulence-enhancing behaviour of polymers in wall flows. *J. Fluid Mech.* 514, 271–280.
- Durst, F., Jovanovic, J., Sender, J., 1995. LDA measurements in the near-wall region of a turbulent flow. *J. Fluid Mech.* 295, 305–335.
- Entov, V.M., Hinch, E.J., 1997. Effect of a spectrum of relaxation times on the capillary thinning of a filament of elastic liquid. *J. Non-Newt. Fluid Mech.* 72, 31–53.
- Escudier, M.P., Presti, F., 1996. Pipe flow of a thixotropic liquid. *J. Non-Newt. Fluid Mech.* 62, 291–306.
- Escudier, M.P., Presti, F., Smith, S., 1999. Drag reduction in the turbulent pipe flow of polymers. *J. Non-Newt. Fluid Mech.* 81, 197–213.
- Graham, M., 2004. Drag reduction in turbulent flow of polymer solutions. *Rheol. Rev.* 2, 143–170.
- Housiadas, K.D., Beris, A.N., 2004. Characteristic scales and drag reduction evaluation in turbulent channel flow of non constant viscosity viscoelastic fluids. *Phys. Fluids* 16 (5), 1581–1586.
- Kim, J., Moin, P., Moser, R., 1987. Turbulence statistics in a fully developed channel flow at low Reynolds number. *J. Fluid Mech.* 177, 133–166.
- Li, C.-F., Gupta, V.K., Sureshkumar, R., Khomami, B., 2004. Polymer induced turbulent drag reduction: a mechanistic study. In: XIVth Int. Congr. Rheology, 222–27 August 2004, Seoul, Korea. Paper NF11 in CD-ROM.
- McKinley, G.H., Sridhar, T., 2002. Filament-stretching rheometry of complex fluids. *Ann. Rev. Fluid Mech.* 34, 375–415.
- Moser, R.D., Kim, J., Mansour, N.N., 1999. Direct numerical simulation of turbulent channel flow up to $Re_\tau = 590$. *Phys. Fluids* 11, 943–945.
- Nagano, Y., Hishida, M., 1987. Improved form of the $k-\epsilon$ model for wall turbulent shear flows. *J. Fluids Eng.* 109, 156.
- Nagano, Y., Shimada, M., 1993. Modeling the dissipation rate equation for two-equation turbulence model. In: 9th Symposium on “Turbulent Shear Flows”, Kyoto, Japan, 16–18th August, paper 23-2.
- Park, T.S., Sung, H.J., 1995. A non-linear low Reynolds number $k-\epsilon$ model for separated and reattaching flows—I. Flow field computations. *Int. J. Heat Mass Transfer* 38, 2657–2666.
- Park, T.S., Sung, H.J., Suzuki, K., 2003. Development of a nonlinear near-wall turbulence model for turbulent flow and heat transfer. *Int. J. Heat Fluid Flow* 24, 29–40.
- Patankar, S.V., Spalding, D.B., 1972. A calculation procedure for heat, mass and momentum transfer in three-dimensional parabolic flows. *Int. J. Heat Mass Transfer* 15, 1787–1806.
- Patel, V.C., Rodi, W., Sheuerer, G., 1985. Turbulence models for near wall and low Reynolds number flows: a review. *AIAA J.* 23 (9), 1308–1319.
- Pinho, F.T., 2003. A GNF framework for turbulent flow models of drag reducing fluids and proposal for a $k-\epsilon$ type closure. *J. Non-Newt. Fluid Mech.* 114, 149–184.
- Pinho, F.T., Whitelaw, J.H., 1990. Flow of non-Newtonian fluids in a pipe. *J. Non-Newt. Fluid Mech.* 34, 129–144.
- Presti, F., 2000. Investigation of transitional and turbulent pipe flow of non-Newtonian fluids. PhD thesis, University of Liverpool, UK.
- Ptasinski, P.K., Nieuwstadt, F.T.M., Van Den Brule, B.H.A.A., Hulsen, M.A., 2001. Experiments in turbulent pipe flow with polymer additives at maximum drag reduction. *Flow, Turbulence Combust.* 66, 159–182.
- Ptasinski, P.K., Boersma, B.J., Nieuwstadt, F.T.M., Hulsen, M.A., Van Den Brule, B.H.A.A., Hunt, J.C.R., 2003. Turbulent channel flow near maximum drag reduction: simulation, experiments and mechanisms. *J. Fluid Mech.* 490, 251–291.
- Skelland, A.H.P., 1967. *Non-Newtonian Flow and Heat Transfer*. Wiley, New York.
- Stelter, M., Brenn, G., Yarin, A.L., Singh, R.P., Durst, F., 2000. Validation and application of a novel elongational device for polymer solutions. *J. Rheol.* 44, 595–616.
- Sureshkumar, R., Beris, A.N., Handler, R.A., 1997. Direct numerical simulation of the turbulent channel flow of a polymer solution. *Phys. Fluids* 9, 743–755.
- Walters, K. 1992. Recent developments in rheometry. In: Moldenaers, P., Keunings, R. (Eds.), *Theoretical and Applied Rheology*, Proc. XIth Int. Congr. on Rheology, Brussels, Belgium, August 17–21, pp. 16–23.
- Warholic, M.D., Massah, H., Hanratty, T.J., 1999. Influence of drag reducing polymers on turbulence: effects of Reynolds number, concentration and mixing. *Exp. Fluids* 27, 461–472.
- Vlachogiannis, M., Hanratty, T.J., 2004. Influence of wavy structured surfaces and large scale polymer structures on drag reduction. *Exp. Fluids* 36, 685–700.

- Younis, B.A., 1987. A computer program for two-dimensional turbulent boundary-layer flows. Internal report, Department of Civil Engineering, City University, London, UK.
- Yu, B., Kawaguchi, Y., 2003. Effect of Weissenberg number on the flow structure: DNS study of drag reducing flow with surfactant additives. *Int. J. Heat Fluid Flow* 24, 491–499.
- Yu, B., Li, F., Kawaguchi, Y., 2004. Numerical and experimental investigation of turbulent characteristics in a drag reducing flow with surfactant additives. *Int. J. Heat Fluid Flow* 25, 961–974.
- Zhou, Q., Akhavan, R., 2003. A comparison of FENE and FENE-P dumbbell and chain models in turbulent flow. *J. Non-Newt. Fluid Mech.* 109, 115–155.